



Cite this: *Sustainable Energy Fuels*,
2024, 8, 1448

Enhanced photoelectrochemical hydrogen production *via* linked BiVO₄ nanoparticles on anodic WO₃ nanocoral structures†

Eunoak Park,  JeongEun Yoo* and Kiyoung Lee 

Morphological properties of photoanodes are crucial for improving their photoelectrochemical (PEC) performance. In this study, we fabricated bismuth vanadate (BiVO₄) nanoparticles (NPs) with an optimal size of ~10 nm, as well as nanowires composed of NPs on anodized tungsten trioxide (WO₃) nanocoral structures. The linked BiVO₄ NPs were decorated by spin-coating, with the amount of the BiVO₄ precursor being controlled. Subsequently, the concentrations of Bi and V in the BiVO₄ precursor were determined. An optimized concentration of 0.3 M Bi and V for the linked BiVO₄ NPs/WO₃ nanocoral heterostructure led to enhanced photocurrent density and hydrogen gas-production compared to those of the pristine WO₃ nanocorals, yielding results that were 2.4 times higher. In particular, the incident photon-to-current conversion efficiency value at 410 nm improved by 8.3 times, as the linked BiVO₄ NPs attained efficient absorbance of visible light and a sufficient electron transfer pathway.

Received 29th November 2023

Accepted 24th February 2024

DOI: 10.1039/d3se01545a

rsc.li/sustainable-energy

1. Introduction

Numerous efforts to produce hydrogen energy have been made using renewable energy from solar fuels to address the global energy crisis.^{1–3} In particular, photoelectrochemical water splitting (PEC-WS) has emerged as a promising green engineering approach for generating hydrogen through direct utilization of sunlight.^{4,5} For PEC-WS, metal oxide semiconductors are mostly used as photoelectrodes because of their beneficial bandgap and band positions for photoreactions.⁶ However, metal oxide semiconductor photoanodes face several critical issues, such as reduced solar-to-hydrogen efficiency of PEC-WS, slow surface water oxidation, poor visible light absorption, and fast electron–hole recombination.^{7,8}

Bismuth vanadate (BiVO₄), the most promising metal oxide photoanode material for PEC-WS, has been investigated owing to its intrinsic properties such as abundance, nontoxicity, and low cost.^{9–11} BiVO₄ also satisfies the requirements for an efficient photoanode by providing a narrow bandgap of 2.4 eV with a relatively negative conduction band edge of ~0 V *vs.* the reversible hydrogen electrode (RHE), and having a high optical absorption coefficient (~10⁴–10⁵ cm⁻¹ at *hν* = 2.5–3.5 eV).^{12–14} Despite these advantages, BiVO₄ still suffers from fast recombination of photogenerated electrons and holes because of its

low carrier mobility (~4.4 × 10⁻² cm² V⁻¹ s⁻¹) and short hole diffusion length (~70 nm).^{15,16}

To overcome these drawbacks and enhance the photo efficiency of PEC-WS, BiVO₄ often adopts a type-II heterojunction configuration with two or more n-type semiconductors. At the heterojunction interface between two semiconductors, a wide bandgap material offers a more negative conduction band (CB) edge, allowing electrons to move from the narrow bandgap material to the wide bandgap material.¹⁷ In this context, tungsten trioxide (WO₃) (~2.8 eV) has been considered the most suitable matching material for forming a type II heterojunction with BiVO₄. This is because WO₃ has a superior electron mobility (~12 cm² V⁻¹ s⁻¹), relatively long hole diffusion length (~150 nm), and lower CB edge of +0.41 V *vs.* RHE compared to BiVO₄.^{18–20} To fabricate WO₃ for the configuration of the BiVO₄/WO₃ heterostructure, several simple approaches have been reported such as a hydrothermal method,^{17,21} dip-coating,²² spin-coating,²³ and anodization.²⁴ Among the various methods, the anodization method is an advantageous because W metal as a substrate can provide direct back contact under the WO₃ layer and can form various nanostructures with a high specific surface area by adjusting the anodization conditions (*e.g.*, electrolyte, temperature, applied potential, *etc.*). There is only one reported research study that used anodic WO₃ for fabricating a BiVO₄/WO₃ heterostructure. However, the BiVO₄/WO₃ heterostructure of anodized WO₃ structures and spin-coated BiVO₄ layers has not fulfilled the role of a photoanode for PEC-WS, because the thick BiVO₄ layer (~850 nm) interrupts the mobility of photogenerated electrons from BiVO₄ to WO₃.²⁵ Thus, it is obvious that rapid electron movement is allowed only when BiVO₄ is as thin as a nanolayer or a nanoparticle (NP).¹⁰ In

Department of Chemistry and Chemical Engineering, Inha University, 100 Inha-ro, Michuhol-gu, 22212 Incheon, South Korea. E-mail: kiyoung@inha.ac.kr; JeongEunYoo@inha.ac.kr

† Electronic supplementary information (ESI) available: FE-SEM, droplet schematics, bandgap, H₂ production rate, and EDX data. See DOI: <https://doi.org/10.1039/d3se01545a>



particular, metal oxide NPs have attracted attention in photoelectrochemical reactions as they provide a large reaction area, leading to improved photoreaction efficiency.

In this study, we have investigated how to fabricate BiVO₄ NPs on anodic WO₃. In addition, we developed BiVO₄ NPs linked as nanowires to a WO₃ nanocoral structure. This is the first study on the heterojunction of BiVO₄ NPs and anodic WO₃ nanocorals. The WO₃ nanocoral structures on W metal were fabricated by the anodization method, as previously reported.²² The linked BiVO₄ NPs were formed on the WO₃ nanocorals by the spin-coating method where, instead of deionized water, we employed an ethylene glycol-based solvent as a BiVO₄ precursor for the spin-coating process, since the utilization of the ethylene glycol-based BiVO₄ precursor allows BiVO₄ nanoparticles to form with sizes below 100 nm as supporting particle agglomeration on WO₃ layers during spin-coating. The use of ethylene glycol as the solvent for the BiVO₄ precursor has not been previously reported. Furthermore, we focus on the amount of the BiVO₄ precursor used during spin-coating to construct linked BiVO₄ NPs on WO₃ nanocorals and determine their morphologies, crystal structures, and PEC performances with different precursor amounts. We then optimized the concentration of vanadium (V) in the BiVO₄ precursor and investigated the morphologies, compositional properties, and PEC performance of the heterostructure of the BiVO₄ NPs/WO₃ nanocorals.

2. Experimental

2.1 Materials

The following materials were used as received: ammonium fluoride (NH₄F, ≥ 98%, Sigma Aldrich), sodium sulfate (Na₂SO₄, ≥ 99.9%, Sigma Aldrich), bismuth(III) nitrate pentahydrate (Bi(NO₃)₃·5H₂O, ≥ 98%, Sigma Aldrich), nitric acid (HNO₃, 60%, Samchun Chemicals), ethylene glycol (HOCH₂CH₂OH, 99.5%, Samchun Chemicals), and ammonium metavanadate (NH₄VO₃, 99%, Daejung Chemicals & Metals).

2.2 Preparation of the BiVO₄/WO₃ photoanodes

Tungsten (W) metal (thickness: 0.1 mm, 99.95% purity, Alfa Aesar) was cut into 1.5 × 1.5 cm² and mechanically ground using a 1200 grit soft sandpaper. Next, the W metal was cleaned successively with acetone, ethanol, and deionized (DI) water using an ultrasonicator, and then dried with nitrogen (N₂) gas. W metal was anodized in a 1 M Na₂SO₄ solution containing 0.5 wt% NH₄F at 15 °C. The thickness of WO₃ nanocorals was increased with increase in anodization time from 1 h to 5 h, to approximately 460, 540, 610, 660 and 690 nm, respectively. Among them, WO₃ anodized for 3 h was used as the substrate. During anodization, a constant voltage of 40 V was applied to W using a DC power source (ODA-EX300-4), and current density *versus* time curves were recorded using a Keithley 2000. After anodization, the anodic WO₃ nanocorals were rinsed with DI water and dried with N₂ gas. Heat-treatment was performed in a tubular furnace at 500 °C under an argon (Ar) atmosphere for 2 h to crystallize the anodized WO₃ nanocoral film. Then, the BiVO₄ NPs were decorated onto the WO₃ nanocoral films by spin-coating. The BiVO₄

precursor solution for spin-coating was prepared by dissolving 0.15 (0.3), 0.23 (0.44), 0.3 (0.59), and 0.6 M (1.18) NH₄VO₃ in a mixture of 10 mL HNO₃ and 20 mL ethylene glycol. After complete dissolution, 0.3 M (2.25) Bi(NO₃)₃·5H₂O was added and then the solution was stirred for 30 min. After dropping 5, 10, and 30 μL of the precursor onto the WO₃ substrate, the samples were rested for 1 min so that the precursor penetrates to the bottom of the nanocoral structures. The spin-coating process was performed at 500 rpm for 60 s, 1000 rpm for 30 s, and 3000 rpm for 3 s for the precursor mixture solution and was repeated 3 times. Between each cycle, the BiVO₄/WO₃ samples were heat-treated in a box furnace at 100 °C for 5 min. After the spin-coating process, the samples were annealed at 550 °C under an air atmosphere using the box furnace for 1 h.

2.3 Characterization

The morphologies of the WO₃ and BiVO₄/WO₃ photoanodes were observed using a field-emission scanning electron microscope (FE-SEM, S-4300, Hitachi). To characterize the crystalline structures of the photoanodes, X-ray diffraction (XRD, X'Pert PRO MRD, Phillips) with a Cu-Kα radiation source and field emission transmission electron microscopy (FE-TEM, JEM-2100F, JEOL) were used. Raman scattering measurements (LabRAM HR Evolution, HORIBA) were obtained using 532 nm lasers. The analysis was conducted at the Inha University Core Facility Center for Sustainable Energy.

2.4 Photoelectrochemical measurements

0.5 M Na₂SO₄ solution, silver/silver chloride (Ag/AgCl, 3 M KCl), a Pt mesh, and BiVO₄/WO₃ photoanodes were used as the electrolyte, and reference, counter, and working electrodes, respectively. Photocurrent density, electrochemical impedance spectroscopy (EIS), and hydrogen (H₂) gas production were measured using a potentiostat (VSP, Bio-Logics) and a solar simulator (LCS-100, Oriel Instruments) with a 100 W xenon (Xe) arc lamp (100 mW cm⁻²). To record the photocurrent density, linear sweep voltammetry (LSV) was performed at a scan rate of 5 mV s⁻¹. The obtained potential was converted into a RHE potential using the following equation:

$$E_{\text{RHE}} = E_{\text{Ag/AgCl}} + (0.0591 \times \text{pH}) + E_{\text{Ag/AgCl}}^{\circ}$$

and

$$E_{\text{Ag/AgCl}} (3 \text{ M KCl}) = 0.1976 \text{ V at } 25 \text{ }^{\circ}\text{C}$$

EIS was performed in the range of 30 kHz–10 MHz at 1.23 V *vs.* RHE. To evaluate PEC H₂-gas production at 1.23 V *vs.* RHE, 200 μL gas was taken from the sealed quartz tube reactor every half hour and injected into a gas chromatograph with a TCD detector (GC/MSD 5975C, Agilent Technologies). The incident photon-to-current conversion efficiency (IPCE) was measured at 1.23 V *vs.* RHE using a monochromator (MonoRa200, DONGWOO OPTRON) and various bandpass filters with a Xe lamp (300 W, OMA). The IPCE was calculated using the following equation:



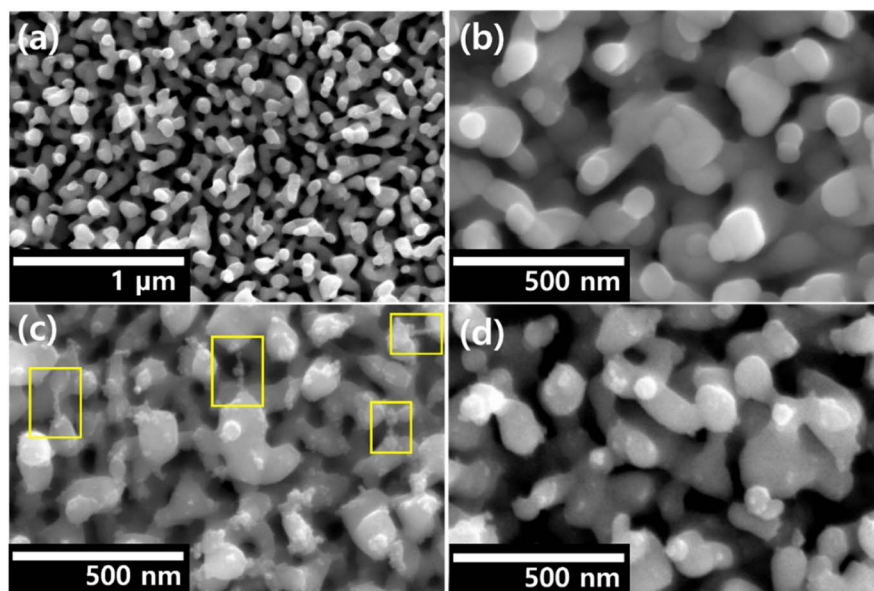


Fig. 1 FE-SEM image of (a) WO_3 nanocorals, (b) 5-BW, (c) 10-BW, and (d) 30-BW.

$$\text{IPCE}(\%) = \frac{hc \times J_{\text{ph}}}{\lambda \times P} \times 100,$$

where h is Planck constant, c is the velocity of light, J_{ph} is the photocurrent density, λ is the incident wavelength, and P is power density of each wavelength.

3. Results and discussion

3.1 Formation of linked BiVO_4 NPs on WO_3 nanocorals

Fig. 1a shows the morphology of WO_3 nanocoral anodized W metal described in our previous report.²⁴ The WO_3 nanocorals have thick branches and round edges with a high surface area, which can support the formation of NPs, and the length of the nanocoral structures is ~ 550 – 600 nm (Fig. S1†). All the $\text{BiVO}_4/\text{WO}_3$ (BW) heterostructures formed by the anodization and spin-coating processes contained BiVO_4 NPs on the WO_3 nanocorals as presented in Fig. 1b–d. During the spin-coating process, the precursor amounts were controlled to be 5, 10, and 30 μL , and the heterostructural BiVO_4 NPs/ WO_3 nanocorals

fabricated with these precursor amounts were labelled as 5-BW, 10-BW, and 30-BW, respectively. Following heat treatment in air, a 5–10 nm size of the well-spread BiVO_4 NPs was observed on the WO_3 nanocorals. The formation of BiVO_4 NPs on the nanocorals was related to the hydrophilicity of the anodic WO_3 nanocorals. After anodization, normally the metal oxide has hydrophilicity.²⁶ The anodic metal oxide is hydrophilic, but the rest of the metal surface is relatively hydrophobic; thus, the precursor prefers to remain on the anodized surface, where it forms a droplet, as shown in Fig. S2.† As the 5 μL precursor amount is a small quantity, it was not sufficient to form numerous BiVO_4 NPs compared to a 10 μL amount, and thus the NPs were rarely located as shown in Fig. 1b. However, a 10 μL precursor droplet can withstand speeds up to 3000 rpm, allowing for a larger quantity of the precursor to remain on the WO_3 nanocoral surface, resulting in a large amount of BiVO_4 NPs being coated on the WO_3 nanocorals for 10-BW. In particular, the NPs are linked as nanowires from one WO_3 nanocoral branch to another, as shown in Fig. 1c. We expected 30-BW to contain more NPs than 10-BW; however, 30-BW displayed only

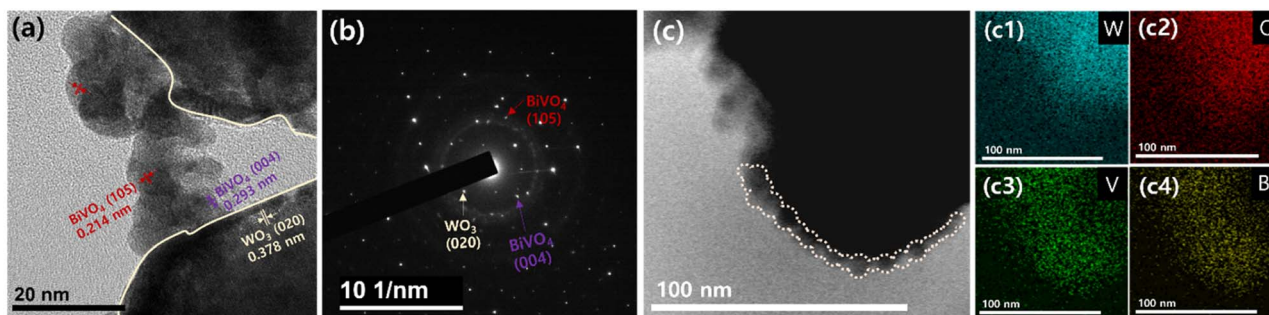


Fig. 2 (a) FE-TEM image of 10-BW, (b) corresponding SAED pattern of (a), (c) TEM image obtained in the HADDF mode of 10-BW, and (c1–c4) corresponding elemental analysis by EDS mapping of W, O, V, and Bi.



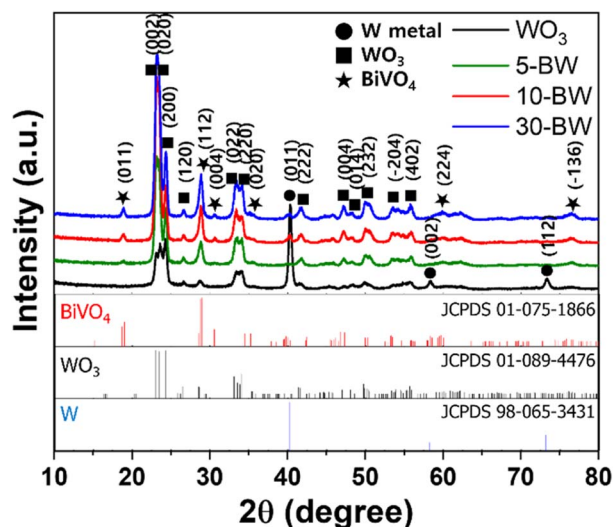


Fig. 3 XRD patterns of WO_3 nanocrystals and $\text{BiVO}_4/\text{WO}_3$ heterostructures of 5-BW, 10-BW, and 30-BW.

well-perched NPs on the WO_3 nanocrystals without linking (Fig. 1d). This is because 30 μL of the precursor is comparatively easy to disperse to the outer area than 10 μL of the precursor when the centrifugal force interacts with the droplet during spin-coating (Fig. S2[†]). In the case where some part of the droplet dispersed to the non-anodized metal surface and the droplet suddenly flattened, the droplet flowed off the substrate, reducing the precursor amount.

The TEM image of 10-BW in Fig. 2a showed ~ 10 nm BiVO_4 NPs with lattice spacings of 0.214 and 0.293 nm representing the planes of (1 0 5) and (0 0 4), respectively, and the WO_3 nanocrystals with a lattice spacing of 0.378 nm, corresponding to the (0 2 0) plane. The selected-area electron diffraction (SAED) pattern (Fig. 2b) confirms a polycrystalline structure; the (0 2 0) plane corresponds to monoclinic WO_3 and the (1 0 5) and (0 0 4) planes correspond to monoclinic BiVO_4 . High-angle annular dark-field (HAADF)-scanning TEM reveals well configured BiVO_4 NPs and WO_3 (Fig. 2c). The NPs were linked to the surface of WO_3 , and energy-dispersive X-ray spectroscopy (EDS) elemental mapping revealed that the BiVO_4 NPs were uniformly distributed on the WO_3 surface.

The crystalline phases of the WO_3 nanocrystals (5-BW, 10-BW, and 30-BW) were examined using XRD, as illustrated in Fig. 3. Peaks corresponding to W metal were observed at 40.2° , 58.2° , and 73.2° for the WO_3 nanocrystals, whereas only the 40.2° peak was observed for the BW samples. The XRD patterns of the WO_3 nanocrystal layer show peaks at 23.0° , 23.5° , 24.2° , 26.5° , 33.1° , 34.0° , 41.6° , 49.9° , and 55.7° indexed to the (0 0 2), (0 2 0), (2 0 0), (1 2 0), (0 2 2), (2 2 0), (2 2 2), (2 3 2), and (4 0 2) planes, respectively. The WO_3 nanocrystals exhibited well-crystallized monoclinic WO_3 phases (JCPDS #089-4476).^{27,28} The XRD patterns of all the BW samples exhibited peaks at 18.9° , 28.9° , 30.5° , 40.2° , 60.0° , and 76.5° corresponding to the (0 1 1), (1 1 2), (0 0 4), (0 2 0), (1 2 1), (2 2 4), and $(-1\ 3\ 6)$ planes, respectively, which are the monoclinic phases of BiVO_4 (JCPDS #075-1866).^{29,30} Although 5-BW showed lower BiVO_4 peak intensities

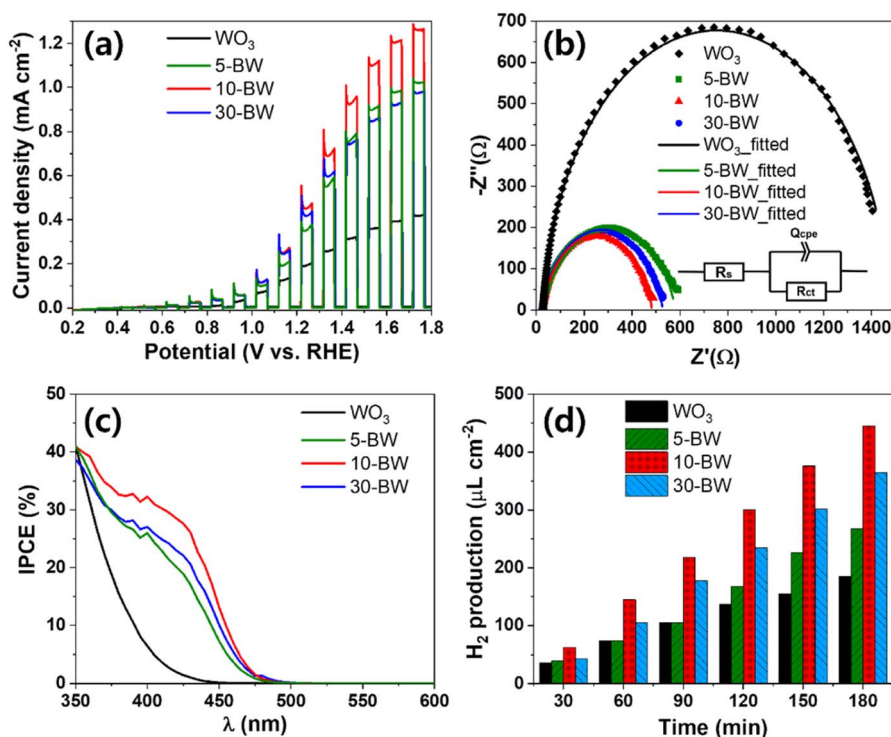


Fig. 4 Photoelectrochemical performances of the WO_3 nanocrystals and $\text{BiVO}_4/\text{WO}_3$ photoanodes of 5-BW, 10-BW, and 30-BW: (a) photocurrent densities by linear sweep voltammetry, (b) Nyquist plots and equivalent circuits, (c) PEC H_2 production diagram as a function of time, and (d) IPCE spectra.



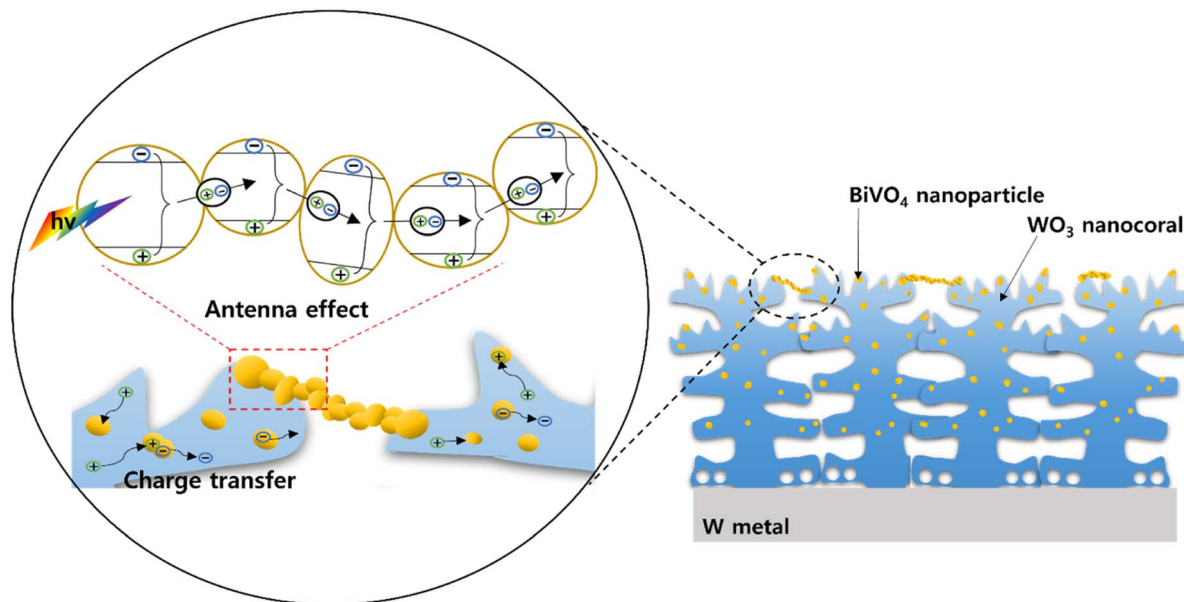


Fig. 5 Schematic illustration of 10-BW and its mechanism of charge transfer and the antenna effect.

at 18.9° and 30.5° owing to the quantity of BiVO_4 , the 10-BW and 30-BW peak intensities were similar. This indicates that $10 \mu\text{L}$ of the BiVO_4 precursor is sufficient to form well-crystallized BiVO_4 NPs that are to be used as photoanodes.

The chopped linear sweep voltammetry (LSV) curves with the PEC performance of 5-BW, 10-BW, and 30-BW are illustrated in Fig. 4a. Compared to the pristine WO_3 nanocorals, all the BW photoanodes exhibited a higher photocurrent density, indicating that the heterostructural BW achieved an improved photocurrent density. The highest photocurrent density of 0.45

mA cm^{-2} at 1.23 V vs. RHE was obtained with the $10 \mu\text{L}$ spin-coated $\text{BiVO}_4/\text{WO}_3$ photoanode, and it was 2.4 times higher than that obtained for the WO_3 nanocorals (0.19 mA cm^{-2} at 1.23 V vs. RHE). The $\text{BiVO}_4/\text{WO}_3$ photoanodes of 30-BW and 5-BW were followed to 0.42 and 0.35 mA cm^{-2} at 1.23 V vs. RHE . The 5-BW sample exhibited the lowest photocurrent density owing to the extremely small quantity of BiVO_4 NPs on the WO_3 layer. The fitted EIS Nyquist plots of the 5-BW, 10-BW, 30-BW, and WO_3 nanocorals are depicted in Fig. 4b. In addition, the applied equivalent circuit consisting of the solution resistance

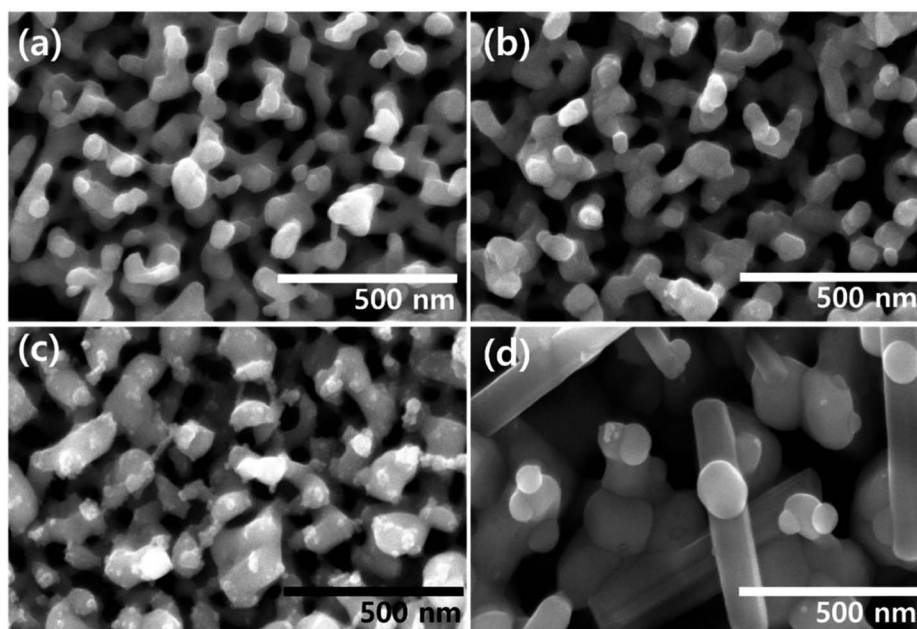


Fig. 6 FE-SEM image of $\text{BiVO}_4/\text{WO}_3$ photoanodes depending on V concentration of the BiVO_4 precursor; (a) 0.15, (b) 0.23, (c) 0.3, and (d) 0.6 M.



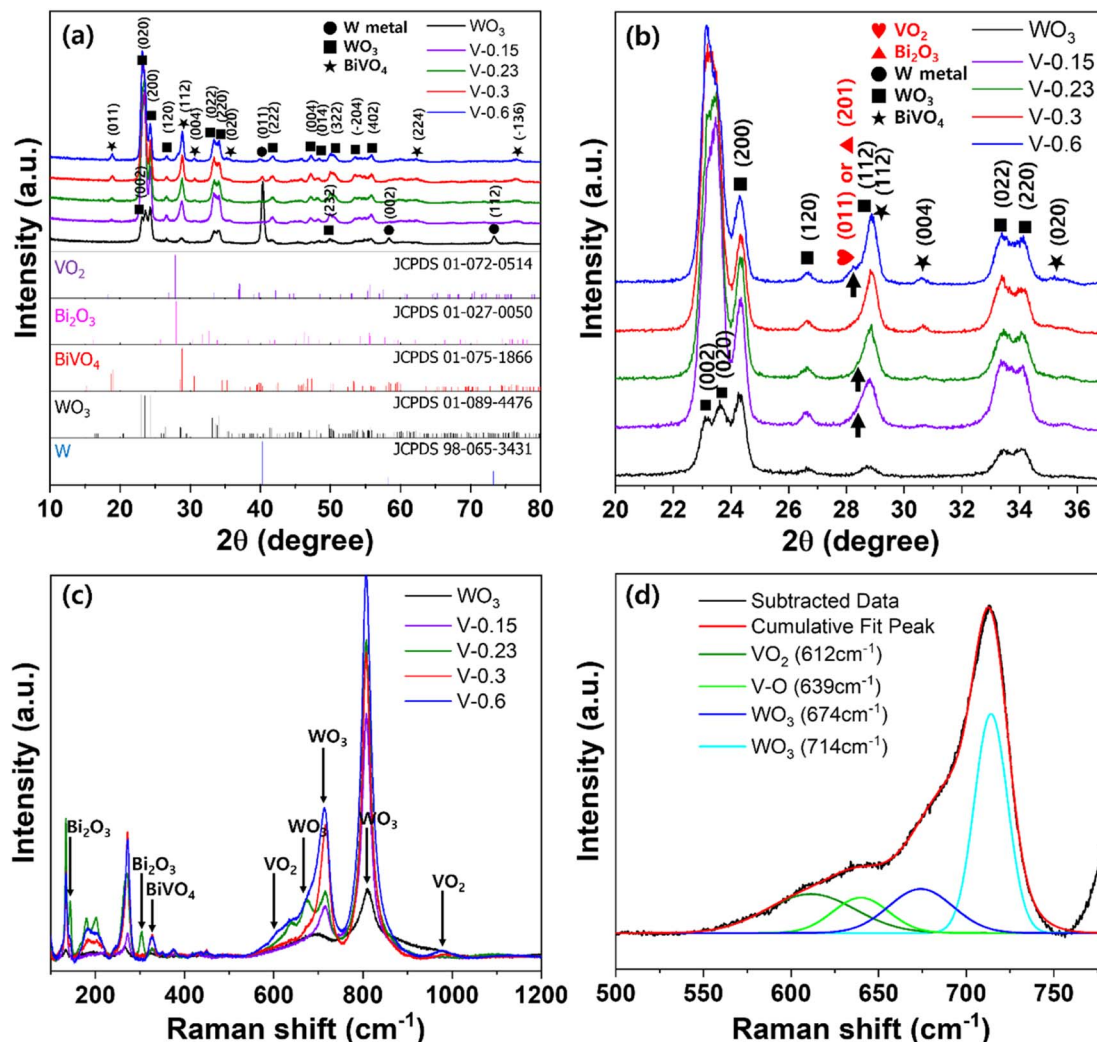


Fig. 7 (a) XRD patterns of $\text{BiVO}_4/\text{WO}_3$, (b) enlargement of (a) from 20° to 37° , (c) Raman spectra of $\text{BiVO}_4/\text{WO}_3$ photoanodes depending on V concentrations of 0.15, 0.23, 0.3, and 0.6 M for the BiVO_4 precursor; and (d) peak separation of V-0.6 at (c) from 500 to 750 cm^{-1} .

(R_s), charge transfer resistance (R_{ct}), and constant phase element (Q_{cpe}) is shown in the inset. The sequence of charge transfer resistance values was in line with the photocurrent densities: 10-BW ($457.3\ \Omega$) < 30-BW ($506.2\ \Omega$) < 5-BW ($561.1\ \Omega$) < WO_3 nanocorals ($1450\ \Omega$). After the PEC measurements, 10-BW showed an identical morphology and crystal structure (Fig. S3–S4[†]). In addition, the chemical composition of each element, except V, displayed identical intensities as illustrated in Fig. S5.[†] The decreased intensity of V is due to dissolution of V^{5+} ions, and the Bi peaks slightly shifted to higher binding energies owing to the strong influence of O bonding energy on Bi after the removal of V. However, this had negligible impact on the changes in performance. As presented in Fig. 4c, the linked BiVO_4 NPs of 10-BW achieved the highest IPCE values of 39% at 360 nm and 30% at 410 nm. At 350 nm, the WO_3 nanocorals, 5-BW, and 10-BW showed an approximate value of 40%, but 10-BW exhibited superior absorbance of light, even at a longer wavelength of 350 nm. The sequence of the IPCE values of the BW samples was 5-BW (36%), 30-BW (35%), and WO_3

nanocorals (31%) at 360 nm; meanwhile, at 410 nm, the order changed to 30-BW (25%), 5-BW (23%), and WO_3 nanocorals (4%). The two IPCE values of 5-BW and 30-BW were reversed at 372 nm, implying that 30-BW absorbed more visible light than 5-BW. Conversely, 5-BW can absorb more UV light than 30-BW. This indicates that a higher absorbance of visible light, instead of UV light, results in an improved PEC efficiency. The bandgaps evaluated using IPCE data are shown in Fig. S6.[†] Even though the amounts of the precursor were significantly different, the bandgaps of the WO_3 nanocorals, 5-BW, 10-BW, and 30-BW were relatively similar, that is, 2.80, 2.54, 2.53, and 2.55 eV, respectively. PEC H_2 -production under solar light irradiation for 3 h is depicted in Fig. 4d. The H_2 amounts of WO_3 nanocorals, 5-BW, 10-BW, and 30-BW were 185.6, 267.6, 445.3, and 365.5 $\mu\text{L cm}^{-2}$, respectively, and they linearly increased with increasing reaction time. H_2 production is interrelated with photocurrent density, and high photocurrent density led to a high production rate; thus 10-BW obtained a higher H_2 production rate of $123.0\ \mu\text{L h}^{-1}\text{ cm}^{-2}$ compared to



30-BW ($86.3 \mu\text{L h}^{-1} \text{cm}^{-2}$) and 5-BW ($33.6 \mu\text{L h}^{-1} \text{cm}^{-2}$), as shown in Fig. S7.† The faradaic efficiency for PEC H_2 -production using the optimal 10-BW was calculated to be 86%. In addition, the mixed structures of BiVO_4 NPs and linked chains of NPs of 10-BW significantly improved the PEC efficiency by providing a charge-transfer pathway for electrons or holes to move easily toward WO_3 or BiVO_4 (Fig. 5). Moreover, the linked BiVO_4 NPs can transfer photon energy from one NP to another, which is called the antenna effect³¹ resulting in high PEC activities. The linked BiVO_4 NPs also connected one WO_3 nanocoral to another during the migration of electron-hole pairs (excitons). Once the exciton is transferred to the WO_3 nanocoral, the exciton is separated into both electron and hole, and the electron/hole transfer is activated.³² Then, each transferred electron migrates to the WO_3 nanocoral, and the holes are transferred to the BiVO_4 NPs. Furthermore, numerous generated excitons increase solar-to-hydrogen conversion efficiency,³³ resulting in the generation of a high amount of H_2 .

3.2 Optimization of the BiVO_4 precursor

To improve the quality of BiVO_4 , V concentrations in the BiVO_4 precursor were controlled to be 0.15, 0.23, 0.3, and 0.6 M, and samples with these concentrations were labelled as V-0.15, V-0.23, V-0.3, and V-0.6, respectively, while the bismuth (Bi) concentration was fixed at 0.3 M. Each precursor was spin-coated on WO_3 nanocorals with 10 μL optimized for PEC performance. Fig. 6 presents the different morphologies of the

BW samples obtained with different V concentrations in the BiVO_4 precursors. In the SEM image of V-0.15 (Fig. 6a), BiVO_4 NPs were not observed, and the morphology was identical to that of the pristine WO_3 nanocorals. BiVO_4 NPs were rarely present in the SEM images of V-0.23, as illustrated in Fig. 6b. Linked BiVO_4 NPs were observed only for V-0.3, as shown in Fig. 6c. The quantity of BiVO_4 NPs increased with an increase in the V concentration from 0.23 M to 0.3 M. However, when the V concentration was increased to 0.6 M, some nanorods are suddenly obtained along with BiVO_4 NPs as shown in Fig. 6d. The nanorods were composed of V and oxygen (O), as shown in Fig. S8.† Vanadium oxide nanorods were formed because of the high concentration of V.

The XRD patterns of the V-controlled $\text{BiVO}_4/\text{WO}_3$ photoanodes are shown in Fig. 7a. The monoclinic phases of WO_3 and BiVO_4 exhibit the same patterns as those shown in Fig. 3. However, all the samples, except V-0.3, demonstrated a broad peak with a strong shoulder peak at approximately 28° , particularly V-0.6 (Fig. 7b). As shown in Fig. 6d, V-0.6 has vanadium oxide nanorods at the surface; thus, the peak at 27.89° was predicted to be of VO_2 (JCPDS #072-0514),³⁴ whereas the lack of V in the V-0.15 or V-0.23 samples could lead to the formation of bismuth oxides, which are responsible for the peak at 27.94° (JCPDS #027-0050).³⁵ As the other peaks of VO_2 or Bi_2O_3 overlapped with the WO_3 or BiVO_4 peaks, additional peaks were not investigated.

Raman scattering measurements were conducted to precisely characterize the V-controlled BiVO_4 (Fig. 7c). The

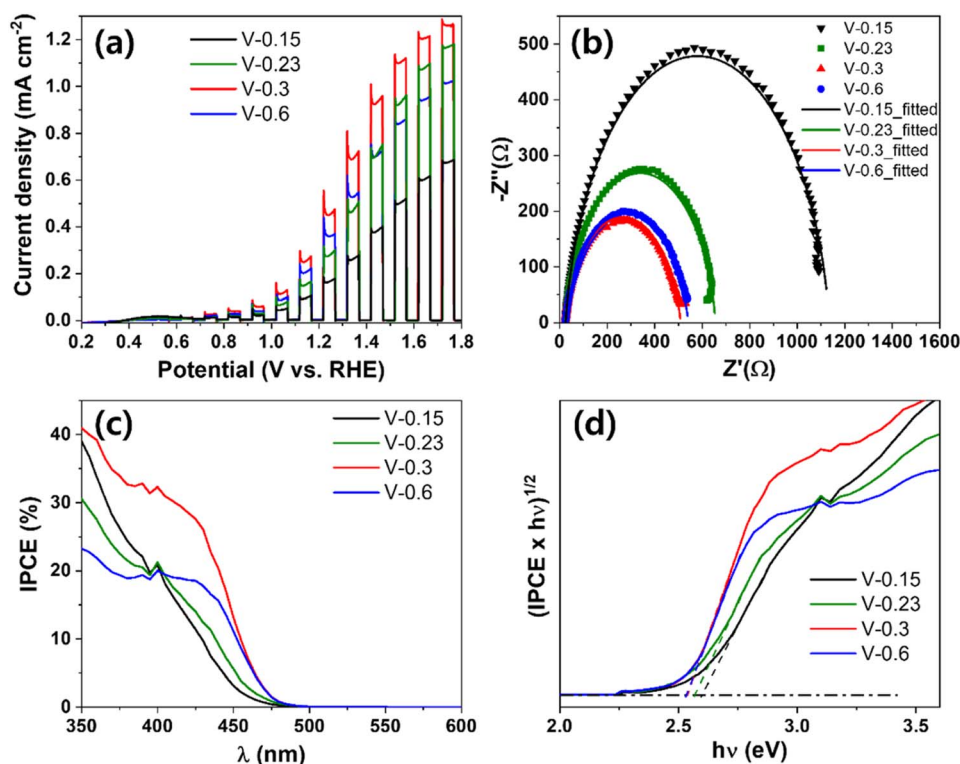


Fig. 8 Photoelectrochemical performances of $\text{BiVO}_4/\text{WO}_3$ photoanodes depending on V concentrations of 0.15, 0.23, 0.3, and 0.6 M of the BiVO_4 precursor; (a) photocurrent densities by linear sweep voltammetry, (b) Nyquist plots, (c) IPCE spectra, and (d) bandgap evaluated by IPCE measurement.



O–W–O stretching bands at 714 and 806 cm^{-1} allowed for the identification of monoclinic WO_3 .³⁶ The peaks for V-0.15 were comparable to those of pristine WO_3 , as the BiVO_4 NPs were rarely present on the surface of the WO_3 nanocorals. After the formation of BiVO_4 , the remaining Bi in the BiVO_4 precursor with V-0.23 formed bismuth oxide. Thus, the peak of Bi–O stretching mode of Bi_2O_3 at 304 cm^{-1} was only observed for V-0.23.³⁷ Similarly, the residue of V in the BiVO_4 precursor with V-0.6 formed vanadium oxide, VO_2 ; thus, the corresponding peaks appeared at 612 and 988 cm^{-1} , as shown in Fig. 6d.^{38,39} As a result, V-0.3 showed BiVO_4 peaks at 326 and 374 cm^{-1} without any by-products, which were attributed to the asymmetric and symmetric deformation of VO_4^{3-} .⁴⁰ Therefore, 0.3 M of Bi and V is an optimal concentration as a BiVO_4 precursor for fabrication of high-quality BiVO_4 NPs.

The PEC performances of different V-controlled $\text{BiVO}_4/\text{WO}_3$ photoanodes are shown in Fig. 8a. The optimal BW photoanode with V-0.3 showed the highest photocurrent density value of 0.45 mA cm^{-2} at 1.23 V vs. RHE. The V-0.6 and V-0.23 samples then followed with photocurrent densities of 0.36 and 0.27 mA cm^{-2} at 1.23 V vs. RHE, and 0.15 M showed an even lower photocurrent density of 0.16 mA cm^{-2} at 1.23 V vs. RHE compared to pristine WO_3 nanocorals. Based on the photocurrent results, the sequence of charge transfer resistance should exhibit an opposite trend: the optimal BW photoanode of V-0.3 had the lowest resistance of 486.9 Ω followed by V-0.9 (518.1 Ω), V-0.44 (633.0 Ω), and V-0.3 (1110 Ω) as shown in Fig. 8b. The equivalent circuit and its components are the same as those shown in Fig. 4b. In Fig. 8c, the optimal BW photoanode (V-0.3) also shows the highest IPCE value of 29% at 420 nm. The order of the IPCE values for V-0.9 (19%), V-0.44 (15%), and V-0.3 (13%) at 420 nm is in line with the PEC results, proving that absorbing a high proportion of visible light remarkably enhances the PEC efficiency. For the evaluated bandgap from the IPCE values in Fig. 8d, the V-0.3 and V-0.44 samples showed bandgap values of 2.60 and 2.57 eV, and the V-0.3 and V-0.9 samples showed the same bandgap value of 2.53 eV. Nevertheless, V-0.9 showed a lower PEC performance than V-0.3 due to low IPCE efficiency in the range of 350 to 450 nm.

4. Conclusions

In summary, this study addressed the formation of heterostructured BiVO_4 and WO_3 with a mixed structure of NPs and linked BiVO_4 NPs on WO_3 nanocoral structures to enhance PEC performance. The linked BiVO_4 NPs were simply constructed on anodic WO_3 nanocorals by controlling the amount of the BiVO_4 precursor to be 10 μL during spin-coating. This phenomenon was related to the hydrophilicity of the WO_3 nanocorals, as the precursor amount on the WO_3 nanocorals that could withstand a high speed rpm during spin-coating was important. Furthermore, the linked BiVO_4 NPs/ WO_3 nanocoral heterostructure showed improved PEC performance, including photocurrent density, PEC H_2 production, and IPCE, compared to the BiVO_4 NPs/ WO_3 nanocoral heterostructure. The linked NPs on the WO_3 nanocorals provided photogenerated electrons to move to the WO_3 substrate and improved the charge carrier and charge separation *via* the antenna effect. Moreover, the NPs did not

fully cover the WO_3 nanocorals, and the nanocoral structures could harvest more light, which allowed for multiple light scattering. The optimized BiVO_4 precursor concentration was 0.3 M of V and Bi, which formed the purest BiVO_4 on the WO_3 nanocorals without any by-product. When the V concentration was lower or higher than the Bi concentration, Bi_2O_3 or VO_2 was formed along with BiVO_4 . Thus, the BW photoanode of the purist V-0.3 allowed realization of the highest photocurrent density and IPCE values of 0.45 mA cm^{-2} (at 1.23 V vs. RHE) and 29% (at 420 nm), respectively, and accordingly the lowest charge transfer resistance of 486.9 Ω .

Conflicts of interest

There are no conflicts to declare.

Acknowledgements

This work was supported by Inha University Research Grant.

References

- 1 Y. Park, K. J. McDonald and K.-S. Choi, *Chem. Soc. Rev.*, 2013, **42**, 2321–2337.
- 2 J. Lee, M. Kim, Y.-T. Kim and J. Choi, *Catal. Today*, 2022, **403**, 67–73.
- 3 K. Min, M. Kim, S. Min, H. Kim and S.-H. Baeck, *Appl. Surf. Sci.*, 2023, **624**, 157117.
- 4 M. Tayebi and B.-K. Lee, *Renewable Sustainable Energy Rev.*, 2019, **111**, 332–343.
- 5 V. S. Kumbhar, H. Lee, J. Lee and K. Lee, *J. Colloid Interface Sci.*, 2019, **557**, 478–487.
- 6 T. Kim, S. S. Patil and K. Lee, *Electrochim. Acta*, 2022, **432**, 141213.
- 7 B. Jin, E. Jung, M. Ma, S. Kim, K. Zhang, J. I. Kim, Y. Son and J. H. Park, *J. Mater. Chem. A*, 2018, **6**, 2585–2592.
- 8 F. F. Abdi, L. Han, A. H. Smets, M. Zeman, B. Dam and R. van de Krol, *Nat. Commun.*, 2013, **4**, 2195.
- 9 J. A. Seabold and K.-S. Choi, *J. Am. Chem. Soc.*, 2012, **134**, 2186–2192.
- 10 Y. Zhou, L. Zhang, L. Lin, B. R. Wygant, Y. Liu, Y. Zhu, Y. Zheng, C. B. Mullins, Y. Zhao, X. Zhang and G. Yu, *Nano Lett.*, 2017, **17**, 8012–8017.
- 11 X. Yao, D. Wang, X. Zhao, S. Ma, P. S. Bassi, G. Yang, W. Chen, Z. Chen and T. Sritharan, *Energy Technol.*, 2018, **6**, 100–109.
- 12 P. Lianos, *Appl. Catal., B*, 2017, **210**, 235–254.
- 13 Y. Pihosh, I. Turkeyvych, K. Mawatari, T. Asai, T. Hisatomi, J. Uemura, M. Tosa, K. Shimamura, J. Kubota, K. Domen and T. Kitamori, *Small*, 2014, **10**, 3692–3699.
- 14 S. S. Patil, J. Lee, E. Park, L. R. Nagappagari and K. Lee, *ACS Appl. Energy Mater.*, 2021, **4**, 13636–13645.
- 15 K. Fuku and K. Sayama, *Chem. Commun.*, 2016, **52**, 5406–5409.
- 16 J. Wang, T. Zhou, Y. Zhang, L. Li, C. Zhou, J. Bai, J. Li, H. Zhu and B. Zhou, *ACS Appl. Mater. Interfaces*, 2022, **14**, 45392–45402.



- 17 E. Park, S. S. Patil, H. Lee, V. S. Kumbhar and K. Lee, *Nanoscale*, 2021, **13**, 16932–16941.
- 18 B.-R. Huang, T.-C. Lin and Y.-M. Liu, *Sol. Energy Mater. Sol. Cells*, 2015, **133**, 32–38.
- 19 G. Zheng, J. Wang, H. Liu, V. Murugadoss, G. Zu, H. Che, C. Lai, H. Li, T. Ding, Q. Gao and Z. Guo, *Nanoscale*, 2019, **11**, 18968–18994.
- 20 J. Su, L. Guo, N. Bao and C. A. Grimes, *Nano Lett.*, 2011, **11**, 1928–1933.
- 21 A. A. M. Ibrahim, I. Khan, N. Iqbal and A. Qurashi, *Int. J. Hydrogen Energy*, 2017, **42**, 3423–3430.
- 22 Q. pan, H. Zhang, Y. Yang and C. Cheng, *Small*, 2019, **15**, 1900924.
- 23 P. Chatchai, S. Kishioka, Y. Murakami, A. Y. Nosaka and Y. Nosaka, *Electrochim. Acta*, 2010, **55**, 592–596.
- 24 E. Park, T. Kim, J. Yoo and K. Lee, *Inorg. Chim. Acta*, 2023, **554**, 121538.
- 25 L. Xia, J. Bai, J. Li, Q. Zeng, X. Li and B. Zhou, *Appl. Catal., B*, 2016, **183**, 224–230.
- 26 J. Lee, S.-Y. Jung, V. S. Kumbhar, S. Uhm, H.-J. Kim and K. Lee, *Catal. Today*, 2021, **359**, 50–56.
- 27 L. Zhang, H. Zhang, B. Wang, X. Huang, Y. Ye, R. Lei, W. Feng and P. Liu, *Appl. Catal., B*, 2019, **244**, 529–535.
- 28 M. Saleem, M. F. Al-Kuhaili, S. M. A. Durrani, A. H. Y. Hendi, I. A. Bakhtiari and S. Ali, *Int. J. Hydrogen Energy*, 2015, **40**, 12343–12351.
- 29 N. Ghazkoob, M. Zargar Shoushtari, I. Kazeminezhad and S. M. Lari Baghal, *J. Alloys Compd.*, 2022, **900**, 163467.
- 30 T. G. U. Ghobadi, A. Ghobadi, M. C. Soydan, M. B. Vishlaghi, S. Kaya, F. Karadas and E. Ozbay, *ChemSusChem*, 2020, **13**, 2577–2588.
- 31 C.-y. Wang, C. Böttcher, D. W. Bahnemann and J. K. Dohrmann, *J. Mater. Chem.*, 2003, **13**, 2322–2329.
- 32 G.-C. Fan, H. Zhu, Q. Shen, L. Han, M. Zhao, J.-R. Zhang and J.-J. Zhu, *Chem. Commun.*, 2015, **51**, 7023–7026.
- 33 Y. Yan, R. W. Crisp, J. Gu, B. D. Chernomordik, G. F. Pach, A. R. Marshall, J. A. Turner and M. C. Beard, *Nat. Energy*, 2017, **2**, 17052.
- 34 L. Zhao, L. Miao, C. Liu, C. Li, T. Asaka, Y. Kang, Y. Iwamoto, S. Tanemura, H. Gu and H. Su, *Sci. Rep.*, 2014, **4**, 7000.
- 35 S. Wang, P. Chen, Y. Bai, J.-H. Yun, G. Liu and L. Wang, *Adv. Mater.*, 2018, **30**, 1800486.
- 36 F. Can, X. Courtois and D. Duprez, *Catalysts*, 2021, **11**, 703.
- 37 M. G. Yañez-Cruz, M. Villanueva-Ibáñez, F. Méndez-Arriaga, C. A. Lucho-Constantino, M. d. I. Á. Hernández-Pérez, M. d. R. Ramírez-Vargas and M. A. Flores-González, *J. Anal. Sci. Technol.*, 2022, **13**, 52.
- 38 I. Derkaoui, M. Khenfouch, I. Boukhoubza, M. Achehboune, R. Hatel, B. M. Mothudi, I. Zorkani, A. Jorio and M. Maaza, *Appl. Phys. A*, 2021, **127**, 934.
- 39 M. Wan, M. Xiong, S. Tian, X. Chen, B. Li, X. Lu and X. Zhao, *Materials*, 2023, **16**, 208.
- 40 M. R. d. S. Pelissari, N. F. Azevedo Neto, L. P. Camargo and L. H. Dall'Antonia, *Electrocatalysis*, 2021, **12**, 211–224.

